OPTICS

Generation and characterization of focused helical x-ray beams

Lars Loetgering[1,2]*, Margarita Baluktsian[3], Kahraman Keskinbora[3], Roarke Horstmeyer[4], Thomas Wilhein[5], Gisela Schütz[3], Kjeld S. E. Eikema[1,2], Stefan Witte[1,2]*

The phenomenon of orbital angular momentum (OAM) affects a variety of important applications in visible optics, including optical tweezers, free-space communication, and 3D localization for fluorescence imaging. The lack of suitable wavefront shaping optics such as spatial light modulators has inhibited the ability to impart OAM on x-ray and electron radiation in a controlled way. Here, we report the experimental observation of helical soft x-ray beams generated by holographically designed diffractive optical elements. We demonstrate that these beams rotate as a function of propagation distance and measure their vorticity and coherent mode structure using ptychography. Our results establish an approach for controlling and shaping of complex focused beams for short wavelength scanning microscopy and OAM-driven applications.

INTRODUCTION

Control over the properties of optical beams has been a driving force for advances in microscopy. Shaping light involves two main ingredients: First, optical elements engineered to redirect radiation, and second, wavefront sensing techniques to assess the performance of these elements and provide feedback for improved fabrication. While this two-step design procedure has pushed visible light microscopes to subwavelength spatial resolution, radiation beyond the visible spectrum is harder to control and monitor (*1*). In particular, microscopes operating with x-ray and extreme ultraviolet radiation do not provide wavelength-scale spatial resolution, in contrast to their visible counterparts (*2*). However, the past decade has seen remarkable progress in both nanofabrication and wavefront sensing at short wavelengths. For example, new nanofabrication techniques based on helium ion beam lithography can now achieve sub–10-nm patterning resolution (*3*). Likewise, wavefront sensing at short wavelengths has been transformed by the emergence of ptychographic coherent diffraction imaging (PCDI) (*4*), which is rapidly becoming a standard technique for high-resolution microscopy with coherent x-rays (*5*, *6*). Primarily used for imaging across large samples at sub–20-nm spatial resolution (*7*, *8*), ptychography can also be harnessed for wavefront sensing and beam characterization (*5*, *9*–*12*). While alternative wavefront sensing approaches based on the transport of intensity equation (*13*, *14*) suffer from singular behavior and nonuniqueness in the presence of vortices in a wave field (*15*, *16*), PCDI has been demonstrated to solve this problem by scanning an object laterally through a beam (*10*). In the latter reference, the authors applied PCDI to characterize pure Laguerre-Gauss (LG) modes.

In this work, we use specially designed binary diffractive optical elements (DOEs) to synthesize superpositions of LG modes that exhibit rotating intensity distributions, also known as "helical beams" (*17*). Such beams have previously been used within the fields of free-space communication, computational imaging with enhanced depth resolution, and optical tweezers (*18*–*21*). In the x-ray community, vortex beams have been generated by means of spiral phase plates and experimentally studied using interferometry (*14*). Spiral zone plates (ZPs) have found application in edge-enhanced x-ray full field microscopy (*22*). Special cases of LG modes are predicted to exhibit orbital angular momentum (OAM)–induced x-ray magnetic dichroism (*23*). Recent work demonstrated time-dependent OAM in extreme ultraviolet beams, resulting in self-torque (*24*). By showing that it is indeed possible to generate high-quality rotating beams in the x-ray spectrum, we enable the extension of important OAM applications from the visible domain into the short-wavelength spectral range. Likewise, by demonstrating that PCDI can be used to accurately measure the phase, vorticity, and spatial coherence structure of these complex fields, we hope to encourage future studies in both the visible and short-wavelength domains to consider PCDI for accurate beam characterization.

Designing diffractive optics for helical soft x-ray beam generation

We designed custom binary diffractive elements to create rotating soft x-ray beams to serve as input beams in ptychography experiments. In what follows, LG modes in polar coordinates (ρ, ϕ) are defined (*16*) as

$$E_n^m(\rho,\phi) = \sqrt{\frac{2n!}{\pi w_0^2(|m|+n)!}} R_n^m(\rho)\, e^{im\phi} \quad (1)$$

where the radial functional dependence R_n^m is given by

$$R_n^m(\rho) = \left(\frac{\sqrt{2}\rho}{w_0}\right)^{|m|} L_n^m\left(\frac{2\rho^2}{w_0^2}\right) e^{\frac{-\rho^2}{w_0^2}} \quad (2)$$

Here, L_n^m are associated Laguerre functions, w_0 is the beam waist, and the integers m and n are the azimuthal and radial order ranging from $-\infty$ to ∞ and from 0 to ∞, respectively. Linear combinations of LG modes with constant ratios of $\Delta n = n_{j+1} - n_j$ and $\Delta m = m_{j+1} - m_j$ give rise to beams with transverse intensity distributions that rotate as a function of propagation distance (*17*, *25*). In the following experiments, we present results with two different rotating focal spot distributions, which differ in the expansion coefficients in the LG decomposition. Both manufactured ZPs are shown in Fig. 1 (A and B). The first beam (green, ZP_1) was chosen as a linear

[1]Advanced Research Center for Nanolithography, Science Park 106, 1098 XG Amsterdam, Netherlands. [2]Vrije Universiteit, De Boelelaan 1081, 1081 HV Amsterdam, Netherlands. [3]Max Planck Institute for Intelligent Systems, Heisenbergstraße 3, 70569 Stuttgart, Germany. [4]Duke University, 101 Science Drive, Durham, NC 27708, USA. [5]University of Applied Science Koblenz, Institute for X-Optics, Joseph-Rovan-Allee 2, 53424 Remagen, Germany.
*Corresponding author. Email: l.loetgering@arcnl.nl (L.L.); witte@arcnl.nl (S.W.)

combination of equally weighted LG modes with pairs (m_1, n_1) = (1,1), (3,5), (5,9), (7,13), (9,17). The second beam (turquoise, ZP_2) was composed of (m_2, n_2) = (0,0), (5,1), (10,2), with equal weights. The beams were numerically propagated upstream by the desired focal lengths and superimposed with a reference wave to create a hologram (*26*). Each hologram was thresholded at half its maximum value to preserve only the regions of constructive interference resulting in binary ZP designs (see the Supplementary Materials). These binary ZPs have focal lengths (f) of f_1 = 10 mm and f_2 = 10.4 mm at a beam energy of 1000 eV, diameters (Ø) of $Ø_1$ = 80 μm and $Ø_2$ = 115 μm, and smallest features/outer zones widths (Δx) of Δx_1 = 300 nm and Δx_2 = 31 nm, respectively. The ZPs have central stops with diameters (•) of $•_1$ = 20 μm and $•_2$ = 40 μm. The manufactured ZPs were chosen to have different numerical apertures resulting in different focal plane beam waists with $w_{0,1}$ = 500 nm and $w_{0,2}$ = 120 nm for ZP_1 and ZP_2, respectively. The beam rotation rate is given by

$$\frac{\partial \phi}{\partial \hat{z}} = \frac{1}{1+\hat{z}^2}\frac{n_{j+1}-n_j}{m_{j+1}-m_j} \quad (3)$$

where $\hat{z} = z/z_0$ is a normalized axial distance, z is the distance from the beam's focal plane, and $z_0 = \pi w_0^2/\lambda$ is the Rayleigh length (*25*). Thus, both the variation in the nonzero LG coefficients and the Rayleigh length allowed us to experimentally switch between scans for small and large rotation rates. In each respective focal plane, the beams generated by ZP_1 and ZP_2 attain maximum rotation rates of 2 and $^1/_5$ rad, respectively. The parameters for both ZPs are summarized in the Supplementary Materials. The above parameters resulted in efficiencies, measured as the integrated squared modulus of the focal plane beam divided by the integrated squared modulus of the beam incident on the ZP area, of 8.0 and 4.2% for ZP_1 and ZP_2, respectively. The difference in these efficiencies is mainly due to the presence of the larger central stop in ZP_2, which partially blocks the transmission of the (m, n) = (0,0) LG mode (see the Supplementary Materials). The holographic approach adapted here requires spatial sampling of the ZPs at least at the Nyquist rate, which leads to practical fabrication limits discussed further below. Moreover, the nonlinear operations involved perturb the experimentally observed beam from the target beam (see the Supplementary Materials). Simulations on alternative ZP design schemes have been reported to mitigate these perturbations at the cost of efficiency (*27*).

Experimental setup for beam characterization

The experimental setup consists of a conventional scanning transmission x-ray microscope, with the addition of our custom DOEs. Figure 1C depicts the UE46-PGM2 beamline of Berlin Electron Storage Ring Society for Synchrotron Radiation (BESSY II) (Helmholtz Zentrum Berlin) and the MAXYMUS (magnetic x-ray microscope with ultrahigh vacuum spectroscopy) scanning microscope. First, a partially coherent x-ray beam (150 to 1900 eV) is spectrally filtered through crossed exit slits (80 μm × 80 μm), resulting in an energy resolution of $E/\Delta E \sim 10^3$ (*28*). The ZPs were positioned 3 m downstream of the exit

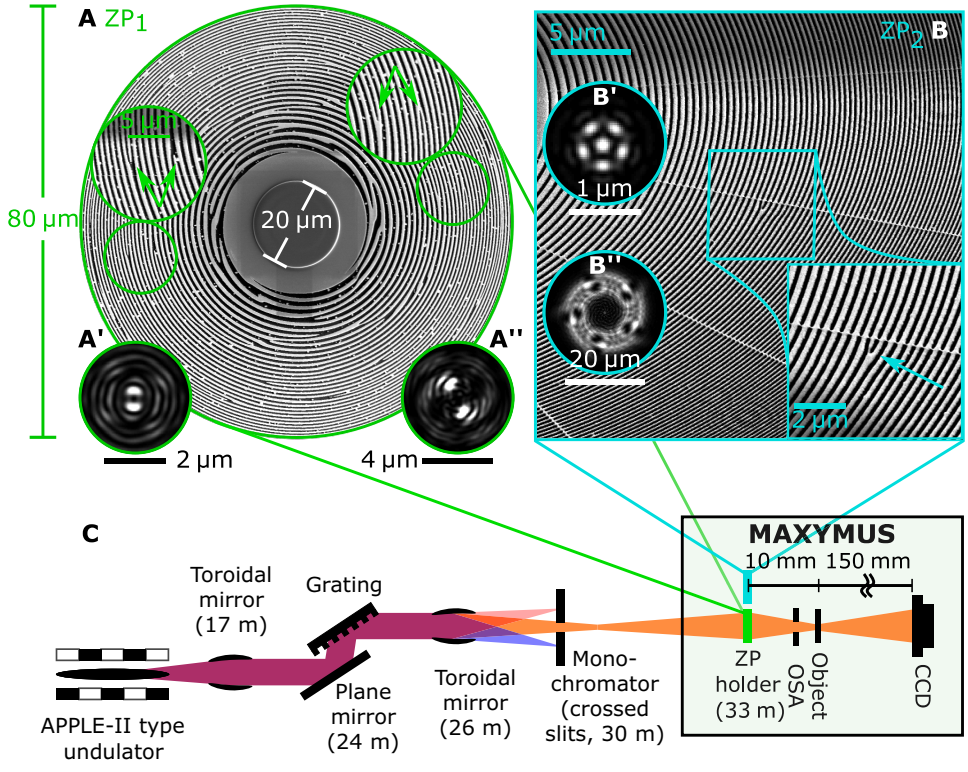

Fig. 1. Experimental setup and fabricated ZPs. (**A**) Scanning electron microscopy (SEM) image of fabricated ZP_1. (**A′**) and (**A″**) show the simulated beam intensities in and 1000 μm downstream the focal plane, respectively, of ZP_1. (**B**) SEM image of the fabricated ZP_2. Because of the large ratio between ZP_2's diameter and feature sizes, only partial SEM views are shown for clarity. (**B′**) and (**B″**) show the simulated beam intensities in and 1000 μm downstream the focal plane, respectively, of ZP_2. The arrows in the insets in all panels show vortex locations in the original beam design that were converted into pitchfork-shaped structures via binary thresholding. (**C**) UE46-PGM2 beamline and MAXYMUS scanning microscope at the BESSY II synchrotron facility. OSA, order sorting aperture; CCD, charge-coupled device.

slits to focus the incident radiation onto test specimens mounted on an interferometer-controlled *xy* translation stage close to the focal plane. An order sorting aperture (OSA) of 25-μm-diameter filters out unwanted radiation from higher diffraction orders of the ZP. A charge-coupled device camera (256 × 256 pixels,48 μm pixel size) is placed 16 cm downstream of the specimen plane to capture the diffraction patterns generated by the interaction of the rotating beam and the test specimen at a number of different scan positions. The set of diffraction patterns captured for each test target form our ptychography datasets.

RESULTS

Ptychographic reconstruction of helical soft x-ray beams

We characterized the focused x-ray radiation from both ZPs by means of ptychography. Two different test samples were chosen to analyze the beams. First, we used a spokes target (i.e., Siemens star), since its large range of spatial frequencies allows us to assess the spatial resolution of the setup in a standardized manner (*29*). Using Fourier ring correlation analysis (*30*), we estimate the half-period spatial resolution in our reconstructions to be between 25 and 31 nm at an energy of 500 eV (see the Supplementary Materials). Second, a lamella taken from an integrated circuit was used to demonstrate the rotating beams' imaging capability in an applied context. The lamella consists of mainly two regions alternating between 80- and 800-nm thickness. To increase the transmissivity at the thicker cross-sectional regions, the integrated circuit was imaged at an energy of 1000 eV. Figure 2 shows the reconstructed test objects and beams for ZP_1 (left column) and ZP_2 (right column). Figure 2A depicts a scanning electron microscopy (SEM) micrograph of the spokes target that was used together with ZP_1. A ptychographic scan in a square region of interest of roughly 15 μm × 15 μm (green inset) was carried out with a linear overlap between adjacent scan positions of 90% (cf. Fig. 2B) (*31*). The reconstructed beam intensities numerically propagated to distances of 250, 500, 750, and 1000 μm downstream the focal plane of ZP_1 are shown in Fig. 2 (C to F), demonstrating that the beam undergoes a rotation angle of slightly less than π rad.

A SEM micrograph of the second specimen, the integrated circuit, is shown in Fig. 2G. Here, a square region of interest of roughly 6 μm × 6 μm (turquoise inset) was scanned with a linear overlap of 90%. The ptychographic reconstruction is shown in Fig. 2H. Figure 2 (I to L) shows the intensities of the beam propagated to distances of 250, 500, 750, and 1000 μm downstream the focal plane of ZP_2.

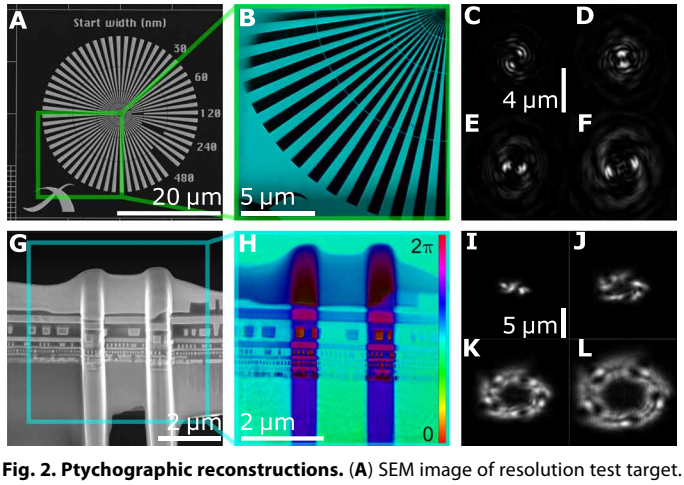

Fig. 2. Ptychographic reconstructions. (**A**) SEM image of resolution test target. (**B**) PCDI reconstruction of the sample in (A). (**C** to **F**) PCDI reconstructed beam intensities at 250, 500, 750, and 1000 μm downstream sample in (A). (**G**) SEM image of integrated circuit. (**H**) PCDI reconstruction of the sample in (G). (**I** to **L**) PCDI reconstructed beam intensities at the same distances downstream the sample in (G) as in (C) to (F). In (B) and (H), brightness and hue correspond to the transmissivity and phase shift of the specimens, respectively.

Retrieving the vorticity of generated helical beams

Given a reconstructed probe beam $P(\boldsymbol{r}) = |P(\boldsymbol{r})| \exp[i\chi(\boldsymbol{r})]$, the angular momentum L and vorticity Ω of the beam can be calculated using the relations $L(\boldsymbol{r}) = \boldsymbol{r} \times J(\boldsymbol{r})$ and $\Omega(\boldsymbol{r}) = \nabla \times J(\boldsymbol{r})$, respectively, where $J(\boldsymbol{r}) = |P(\boldsymbol{r})|^2 \nabla \chi(\boldsymbol{r})$ is the optical current associated with the beam (*32*). The vorticity is proportional to the torque acting on a small particle placed in the beam and, as opposed to the angular momentum, is independent of the choice of coordinate system. Figure 3 shows the evolution of the helical beam (ZP_1) along the propagation direction. Figure 3A depicts a three-dimensional (3D) rendering of the central two lobes of the helical beam. Figure 3 (B to G) shows sections of the beam intensity as a function of propagation distance. The *z*-component of the vorticity is shown in Fig. 3 (H to M), where all images share the same scale as indicated in Fig. 3G. The vorticity takes on its largest absolute value around the focal plane (Fig. 3J). In addition, the vorticity inside the helical beam can take on two polarities (red and blue) as opposed to beams produced by spiral ZPs generating pure LG modes (*10*), which have only one polarity.

Spatial coherence analysis

To study the focusing properties of ZP_2 under partially coherent illumination, the exit slits of the beamline were opened up to a size of 100 μm × 100 μm. We selected ZP_2 to generate a partially coherent rotating beam in this experiment owing to its larger diameter. The large exit slit aperture and ZP diameter resulted in significantly lower spatial coherence than investigated in a previous experiment, where a coherence analysis with an exit slit opening of 20 μm × 20 μm and a ZP diameter of 30 μm was reported (*11*). The coherent mode

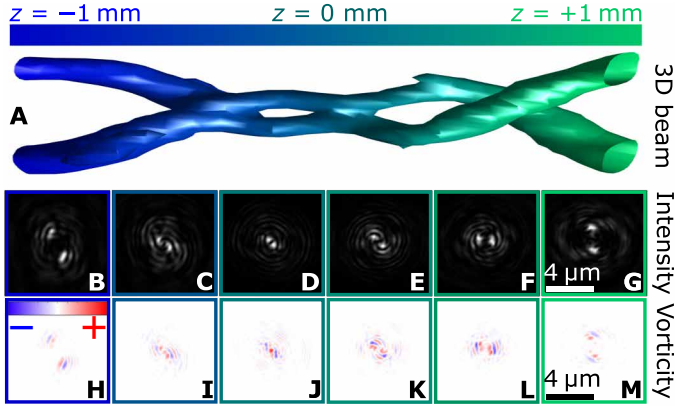

Fig. 3. 3D rotating soft x-ray beam profile and vorticity. (**A**) Central lobes of helical beam intensity along propagation direction as produced by ZP_1. (**B** to **G**) Numerically propagated beam intensities from $z = -1$ mm to $z = +1$ mm around the focal plane. (**H** to **M**) Vorticity for the beams in (B) to (G). (B) to (G) and (H) to (M) share the same spatial dimensions as indicated by the scale bars in (G) and (M). The color bar in (H) indicates the polarity of the vorticity.

structure of the beam produced by ZP_2 was computationally recovered using state mixture ptychography (*33*). The reconstructed coherent modes, after numerical back-propagation into the OSA plane, are depicted in Fig. 4. Figure 4A shows the 9 strongest of 16 reconstructed coherent modes of the partially coherent beam. A common quadratic phase factor present in all coherent modes due to focusing was removed to aid visualization (the quadratic phase was kept for the subsequent spatial coherence analysis). Figure 4B shows the incoherent superposition of all coherent modes in the OSA plane. The beam in the OSA plane is approximately 20 μm in diameter. In the lower right quadrant, the edge of the OSA is visible, indicating that the beam was slightly clipped by the aperture. The decreased intensity contrast as compared to Fig. 2L is due to the incoherent addition of all 16 coherent modes. Figure 4C shows a 1D section through the 4D mutual intensity of the beam, which was calculated from the coherent mode structure in Fig. 4A along the colored lines indicated in Fig. 4B. The mean of the extracted mutual intensity curves exhibits a half width at half maximum of 4.6 μm ± 0.4 μm. This may be interpreted as the characteristic length scale over which two points in the beam are mutually coherent in the OSA plane and under the given exit slit configuration (*34*). The relative energy contained in each coherent mode is shown in Fig. 4D, showing that more than 99% of the relative energy is contained within the first nine coherent modes.

DISCUSSION

An interesting feature of the coherent mode decomposition in the present experiment is that all modes share vortices in the same locations. This is indicated by the white, dotted ellipsoidal regions in Fig. 4A. It follows that the beam's mutual intensity contains vortices in these locations, which are also known as coherence simplices (*35*). A closer inspection reveals that the vortices in Fig. 4A share the same handedness. Thus, the beam carries accumulated vorticity from each individual coherent mode.

Thanks to the completeness of the LG modes, theoretically any wavefront can be synthesized by a linear combination of these basis functions. Practically, wavefront shaping capabilities are limited by nanofabrication techniques for manufacturing the DOE for a given rotating beam profile. In particular, the width of LG modes increases

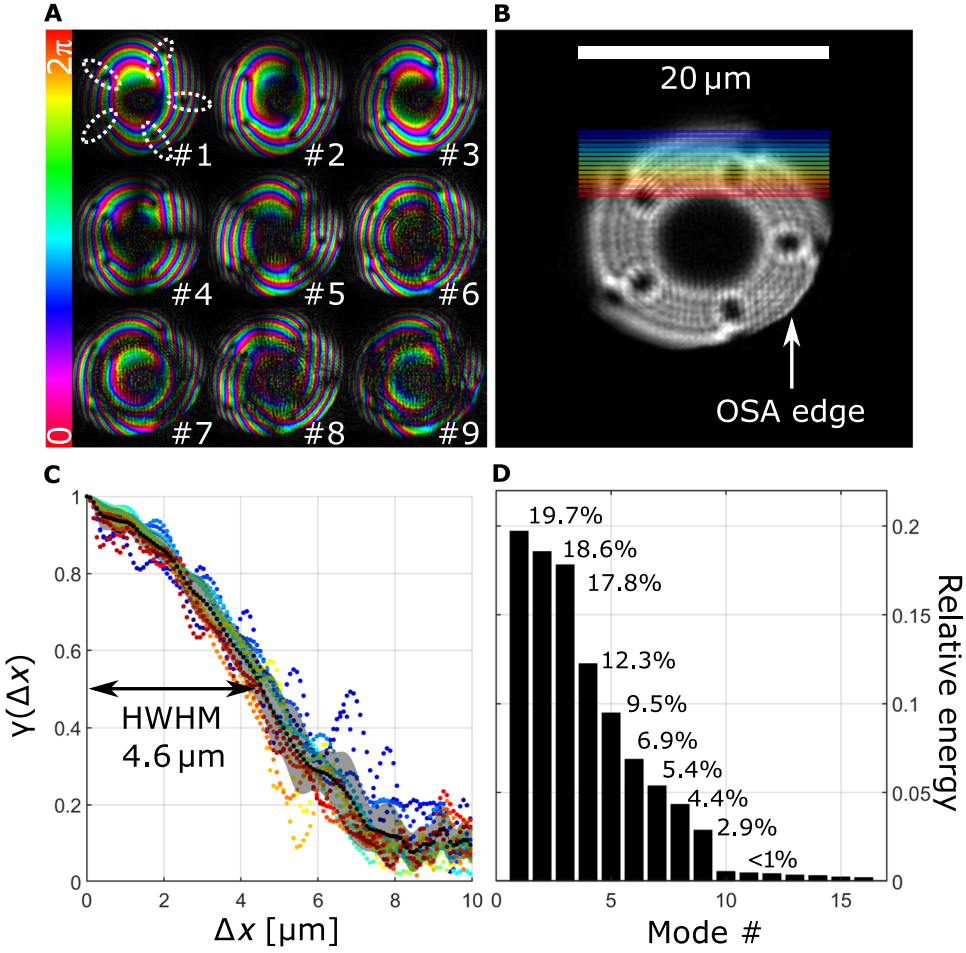

Fig. 4. Coherent mode structure of rotating soft x-ray beam. (**A**) Coherent mode structure of the beam produced by ZP_2 and an exit slit opening of 100 μm × 100 μm: The white ellipsoids show regions containing coherence simplices (hue and brightness represent phase and amplitude, respectively). (**B**) Beam intensity in OSA plane. (**C**) Normalized mutual intensity γ(Δ*x*) computed along the colored lines in (B). The black dotted line shows the average over all coherence curves with 1 SD indicated by the shaded region. (**D**) Relative mode energy versus mode number. The mode numbers in (D) correspond to the numbers (#) indicated in (A). HWHM, half width at half maximum.

with both azimuthal and radial order. More precisely, the beam width σ of LG beams at distance *f* upstream the focal plane is given by (*36*)

$$\sigma(z) = w_0 \left[1 + \left(\frac{\lambda f}{\pi w_0^2}\right)^2\right]^{1/2} \sqrt{m + 2n + 1} \quad (4)$$

Requiring a ZP of diameter Ø to support the beam width of an LG mode leads to the condition Ø ≥ σ or

$$m + 2n + 1 \leq \frac{Ø^2}{w_0^2\left[1 + \left(\frac{\lambda f}{\pi w_0^2}\right)^2\right]} \quad (5)$$

where *f* is the focal length of the ZP. Thus, a finite-sized ZP admits only low-order LG modes. In addition, a large beam diameter potentially results in undersampled far-field diffraction measurements in PCDI experiments. To satisfy the Shannon-Nyquist sampling condition (*37*) in the detector plane, the focal plane spot size w_0 is limited by

$$w_0 \sqrt{m + 2n + 1} \leq \frac{\lambda z}{\Delta q} \quad (6)$$

where Δq is the detector pixel size and *z* is the sample-detector distance. It is noted that the latter condition may be relaxed using detector subsampling methods (*38*). The ZP designs reported here were chosen to comply with both conditions 5 and 6.

The common roadmap in most scanning microscopy techniques is to decrease the diameter of the incident optical beam or scanning probe focus to obtain localized information about a sample under study. In contrast, a unique feature of PCDI is the ability to computationally recover beams and objects with spatial resolution that can be orders of magnitude smaller than the size of the illuminating beam. While this stands out as an advantage of ptychography over classical scanning transmission x-ray and electron microscopy, an open problem is how to use the degrees of freedom gained by using extended beams. A number of studies empirically suggested the advantage of structured and randomized beams (*39*–*43*), arguing the latter result in detector dynamic range advantages. However, there is a large variety in possible structured beam shapes generated from binary DOEs (*27*). The work presented here allows for complex focused beam shaping and precise control over additional functionality such as OAM, a feature not afforded by randomized illuminations. Controlling multiple opposing OAM polarities with a single diffractive optical element may be relevant for OAM-induced x-ray magnetic dichroism studies, since it would allow to study the difference in absorption of photons with opposing OAM in a single ptychographic scan (*23*).

CONCLUSION

In conclusion, we have generated helical soft x-ray beams using DOEs and characterized their properties by means of ptychography. The beams were computationally reconstructed by means of ptychography, affirming its ability for complex wavefront analysis. Theoretical limits that bound the radial and azimuthal order of LG modes generated from DOEs were discussed, as quantified by conditions 5 and 6. The coherent mode structure of a helical beam was analyzed, resulting in the observation of coherence simplices. An interesting future research direction will be to investigate the ability of helical beams to improve multislice ptychographic reconstructions. This route seems promising in light of 3D point source localization applications, where rotating point spread functions have previously been used to enhance the depth resolution in visible light microscopes (*19*, *20*).

MATERIALS AND METHODS

Nanofabrication

The ZPs were fabricated on a 100-nm Au layer sputtered on 50-nm-thick Si_3N_4 membranes. For patterning, a 30-keV Ga^+ focused ion beam (Nova NanoLab 600, FEI) was chosen with a current of 300 pA that results in a nominal beam size of 31 nm. The ZP pattern was written in a single cycle with 30-nm step size and 0.4-ms dwell time, which corresponds to 3.2% overlap and an ion dose of 8.3×10^{16} ions/cm^2. SEM images of the final ZPs are shown in Fig. 1 (A and B). Notably, the vortex locations in the beams resulted in pitchfork-shaped structures as highlighted by the arrows in the insets.

Ptychographic reconstruction algorithm

The reconstruction results shown in Figs. 2 to 4 were obtained using the momentum-accelerated ptychographic iterative engine (mPIE) reported in (*44*). The feedback and friction parameters were chosen to be β = 0.25 and η = 0.9, respectively, for both the probe and the object. The mPIE algorithm was modified to account for partial spatial coherence using the detector plane algorithmic methods reported in the supplementary materials of (*33*). In addition, the measured diffraction data were subsampled by a factor of 2 using the approach reported in (*38*), allowing us to extend the probe field of view in the object plane by the same factor. Working with larger probes has the practical advantage that the number of scan positions can be reduced resulting in accelerated data acquisition speed. For both datasets, the algorithm converged to the final results within 100 iterations.

SUPPLEMENTARY MATERIALS

Supplementary material for this article is available at http://advances.sciencemag.org/cgi/content/full/6/7/eaax8836/DC1

Table S1. Summary of ZP parameters.
Fig. S1. Binary ZP design.
Fig. S2. Mode transfer in binary ZPs.
Fig. S3. Spatial resolution analysis.
Movie S1. Propagation of beam from ZP_1.
Movie S2. Propagation of beam from ZP_2.

REFERENCES AND NOTES

1. D. Attwood, A. Sakdinawat, *Soft X-Rays and Extreme Ultraviolet Radiation* (Cambridge Univ. Press, ed. 2, 2017).
2. A. Sakdinawat, D. Attwood, Nanoscale X-ray imaging. *Nat. Photonics* **4**, 840–848 (2010).
3. M. Melli, A. Polyakov, D. Gargas, C. Huynh, L. Scipioni, W. Bao, D. F. Ogletree, P. J. Schuck, S. Cabrini, A. Weber-Bargioni, Reaching the theoretical resonance quality factor limit in coaxial plasmonic nanoresonators fabricated by helium ion lithography. *Nano Lett.* **13**, 2687–2691 (2013).
4. H. M. L. Faulkner, J. M. Rodenburg, Movable aperture lensless transmission microscopy: A novel phase retrieval algorithm. *Phys. Rev. Lett.* **93**, 023903 (2004).
5. P. Thibault, M. Dierolf, A. Menzel, O. Bunk, C. David, F. Pfeiffer, High-resolution scanning X-ray diffraction microscopy. *Science* **372**, 379–382 (2008).
6. F. Pfeiffer, X-ray ptychography. *Nat. Photonics* **12**, 9–17 (2018).
7. J. Deng, D. J. Vine, S. Chen, Q. Jin, Y. S. Nashed, T. Peterka, S. Vogt, C. Jacobsen, X-ray ptychographic and fluorescence microscopy of frozen-hydrated cells using continuous scanning. *Sci. Rep.* **7**, 445 (2017).

8. Y. Jiang, Z. Chen, Y. Han, P. Deb, H. Gao, S. Xie, P. Purohit, M. W. Tate, J. Park, S. M. Gruner, V. Elser, D. A. Muller, Electron ptychography of 2D materials to deep sub-ångström resolution. *Nature* **559**, 343–349 (2018).
9. A. Schropp, P. Boye, J. M. Feldkamp, R. Hoppe, J. Patommel, D. Samberg, S. Stephan, K. Giewekemeyer, R. N. Wilke, T. Salditt, J. Gulden, A. P. Mancuso, I. A. Vartanyants, E. Weckert, S. Schöder, M. Burghammer, C. G. Schroer, Hard x-ray nanobeam characterization by coherent diffraction microscopy. *Appl. Phys. Lett.* **96**, 091102 (2010).
10. J. Vila-Comamala, A. Sakdinawat, M. Guizar-Sicairos, Characterization of x-ray phase vortices by ptychographic coherent diffractive imaging. *Opt. Lett.* **39**, 5281–5284 (2014).
11. L. Loetgering, M. Rose, K. Keskinbora, M. Baluktsian, G. Dogan, U. Sanli, I. Bykova, M. Weigand, G. Schütz, T. Wilhein, Correction of axial position uncertainty and systematic detector errors in ptychographic diffraction imaging. *Opt. Eng.* **57**, 084106 (2018).
12. Y. Esashi, C.-T. Liao, B. Wang, N. Brooks, K. M. Dorney, C. Hernández-García, H. Kapteyn, D. Adams, M. Murnane, Ptychographic amplitude and phase reconstruction of bichromatic vortex beams. *Opt. Express* **26**, 34007–34015 (2018).
13. L. J. Allen, M. P. Oxley, Phase retrieval from series of images obtained by defocus variation. *Opt. Commun.* **199**, 65–75 (2001).
14. A. G. Peele, K. A. Nugent, A. P. Mancuso, D. Paterson, I. McNulty, J. P. Hayes, X-ray phase vortices: Theory and experiment. *J. Opt. Soc. Am. A.* **21**, 1575–1584 (2004).
15. T. E. Gureyev, A. Roberts, K. A. Nugent, Partially coherent fields, the transport-of-intensity equation, and phase uniqueness. *J. Opt. Soc. Am. A.* **12**, 1942–1946 (1995).
16. G. Gbur, *Singular Optics* (CRC Press, ed. 1, 2016).
17. Y. Y. Schechner, R. Piestun, J. Shamir, Wave propagation with rotating intensity distributions. *Phys. Rev. E.* **54**, R50–R53 (1996).
18. J. Leach, M. J. Padgett, S. M. Barnett, S. Franke-Arnold, J. Courtial, Measuring the orbital angular momentum of a single photon. *Phys. Rev. Lett.* **88**, 257901 (2002).
19. S. R. P. Pavani, M. A. Thompson, J. S. Biteen, S. J. Lord, N. Liu, R. J. Twieg, R. Piestun, W. E. Moerner, Three-dimensional, single-molecule fluorescence imaging beyond the diffraction limit by using a double-helix point spread function. *Proc. Natl. Acad. Sci. U.S.A.* **106**, 2995–2999 (2009).
20. Y. Shechtman, S. J. Sahl, A. S. Backer, W. E. Moerner, Optimal point spread function design for 3D imaging. *Phys. Rev. Lett.* **113**, 133902 (2014).
21. M. Padgett, R. Bowman, Tweezers with a twist. *Nat. Photonics* **5**, 343–348 (2011).
22. A. Sakdinawat, Y. Liu, Soft-x-ray microscopy using spiral zone plates. *Opt. Lett.* **32**, 2635–2637 (2007).
23. M. van Veenendaal, I. McNulty, Prediction of strong dichroism induced by X rays carrying orbital momentum. *Phys. Rev. Lett.* **98**, 157401 (2007).
24. L. Rego, K. M. Dorney, N. J. Brooks, Q. L. Nguyen, C.-T. Liao, J. San Román, D. E. Couch, A. Liu, E. Pisanty, M. Lewenstein, L. Plaja, H. C. Kapteyn, M. M. Murnane, C. Hernández-García, Generation of extreme-ultraviolet beams with time-varying orbital angular momentum. *Science* **364**, eaaw9486 (2019).
25. R. Piestun, Y. Y. Schechner, J. Shamir, Propagation-invariant wave fields with finite energy. *J. Opt. Soc. Am. A.* **17**, 294–303 (2000).
26. E. Di Fabrizio, D. Cojoc, S. Cabrini, B. Kaulich, J. Susini, P. Facci, T. Wilhein, Diffractive optical elements for differential interference contrast x-ray microscopy. *Opt. Express* **11**, 2278–2288 (2003).
27. S. Marchesini, A. Sakdinawat, Shaping coherent x-rays with binary optics. *Opt. Express* **27**, 907–917 (2019).
28. R. Follath, J. S. Schmidt, M. Weigand, K. Fauth, The x-ray microscopy beamline UE46-PGM2 at BESSY. *AIP Conf. Proc.* **1234**, 323–326 (2010).
29. R. Horstmeyer, R. Heintzmann, G. Popescu, L. Waller, C. Yang, Standardizing the resolution claims for coherent microscopy. *Nat. Photonics* **10**, 68–71 (2016).
30. M. van Heel, M. Schatz, Fourier shell correlation threshold criteria. *J. Struct. Biol.* **151**, 250–262 (2005).
31. O. Bunk, M. Dierolf, S. Kynde, I. Johnson, O. Marti, F. Pfeiffer, Influence of the overlap parameter on the convergence of the ptychographical iterative engine. *Ultramicroscopy* **108**, 481–487 (2008).
32. M. V. Berry, Optical currents. *J. Opt. A Pure Appl. Opt.* **11**, 094001 (2009).
33. P. Thibault, A. Menzel, Reconstructing state mixtures from diffraction measurements. *Nature* **494**, 68–71 (2013).
34. E. Wolf, *Introduction to the Theory of Coherence and Polarization of Light* (Cambridge Univ. Press, ed. 1, 2007).
35. T. P. Simula, D. M. Paganin, Coherence simplices. *New J. Phys.* **14**, 113015 (2012).
36. R. L. Phillips, L. C. Andrews, Spot size and divergence for Laguerre Gaussian beams of any order. *Appl. Opt.* **22**, 643–644 (1983).
37. J. W. Goodman, *Introduction to Fourier Optics* (Roberts and Company Publishers, ed. 3, 2004).
38. L. Loetgering, M. Rose, D. Traffer, I. A. Vartanyants, A. Rosenhahn, T. Wilhein, Data compression strategies for ptychographic diffraction imaging. *Adv. Opt. Technol.* **6**, 475–483 (2017).
39. A. M. Maiden, J. M. Rodenburg, M. J. Humphry, Optical ptychography: A practical implementation with useful resolution. *Opt. Lett.* **35**, 2585–2587 (2010).
40. M. Guizar-Sicairos, M. Holler, A. Diaz, J. Vila-Comamala, O. Bunk, A. Menzel, Role of the illumination spatial-frequency spectrum for ptychography. *Phys. Rev. B* **86**, 100103 (2012).
41. A. M. Maiden, G. R. Morrison, B. Kaulich, A. Gianoncelli, J. M. Rodenburg, Soft X-ray spectromicroscopy using ptychography with randomly phased illumination. *Nat. Commun.* **4**, 1669 (2013).
42. G. R. Morrison, F. Zhang, A. Gianoncelli, I. K. Robinson, X-ray ptychography using randomized zone plates. *Opt. Express* **26**, 14915 (2018).
43. M. Odstrčil, M. Lebugle, M. Guizar-Sicairos, C. David, M. Holler, Towards optimized illumination for high-resolution ptychography. *Opt. Express* **27**, 14981–14997 (2019).
44. A. Maiden, D. Johnson, P. Li, Further improvements to the ptychographical iterative engine. *Optica* **4**, 736–745 (2017).

Acknowledgments: We thank M. Weigand for technical support, T. Alieva and J. A. Rodrigo for useful discussions, and C. Ozsoy-Keskinbora and D. C. Bell for providing the FIB lamella of the integrated circuit. **Funding:** This research was supported by the Nederlandse Organisatie voor Wetenschappelijk Onderzoek (NWO-HTSM project nr. 13934) and the European Research Council (ERC Starting Grant 637476). **Author contributions:** L.L. conceived the idea and the ZP design, wrote the ptychography software, and carried out the data analysis. M.B. optimized the patterning process, wrote the script that synthesizes the Graphic Database System (GDSII) pattern files, and fabricated the ZPs. M.B., L.L., and K.K. carried out the experiment. L.L., S.W., and R.H. wrote the manuscript. S.W., K.S.E.E., T.W., K.K., and G.S. supervised the research. All authors discussed the results and contributed in editing the manuscript. **Competing interests:** The authors declare that they have no competing interests. **Data and materials availability:** All data needed to evaluate the conclusions in the paper are present in the paper and/or the Supplementary Materials. Additional data related to this paper may be requested from the authors.

Submitted 8 May 2019
Accepted 26 November 2019
Published 14 February 2020
10.1126/sciadv.aax8836

Citation: L. Loetgering, M. Baluktsian, K. Keskinbora, R. Horstmeyer, T. Wilhein, G. Schütz, K. S. E. Eikema, S. Witte, Generation and characterization of focused helical x-ray beams. *Sci. Adv.* **6**, eaax8836 (2020).

Generation and characterization of focused helical x-ray beams

Lars Loetgering, Margarita Baluktsian, Kahraman Keskinbora, Roarke Horstmeyer, Thomas Wilhein, Gisela Schütz, Kjeld S. E. Eikema and Stefan Witte

Sci Adv **6** (7), eaax8836.
DOI: 10.1126/sciadv.aax8836